Front. Chem. Sci. Eng. 2025, 19(4): 26
https://doi.org/10.1007/s11705-025-2527-4

RESEARCH ARTICLE

Selective C–C coupling via copper atom reconfiguration in CO_2 electroreduction

**Linlin Zhou[1], Yang Zhong[2], Kai Sun[3], Benqiang Tian[1], Haoyang Wu[1], Wei Liu[1], Tong Wan[1],
Huijun Xin[4], Chen Deng[5], Xiaojie Li[5], Jinjie Fang[5], Geoffrey I.N. Waterhouse[3],
Yun Kuang (✉)[4], Daojin Zhou (✉)[1], Xiaoming Sun (✉)[1]**

1 State Key Laboratory of Chemical Resource Engineering, Beijing University of Chemical Technology, Beijing 100029, China
2 Weichai Power Co., Ltd., Weifang 261061, China
3 School of Chemical Sciences, the University of Auckland, Auckland 1010, New Zealand
4 Ocean Hydrogen Energy R & D Center, Research Institute of Tsinghua University in Shenzhen, Shenzhen 518057, China
5 PetroChina Shenzhen New Energy Research Institute Co., Ltd., Shenzhen 518052, China

Abstract Copper-based catalysts play a pivotal role in CO_2 electroreduction (CER) toward multi-carbon (C_{2+}) products. However, achieving a high selectivity for C_{2+} products remains a formidable challenge. In this work, a facile electrochemical oxidation-reduction technique was developed to modulate the surface morphology of a copper foil using sulfur and oxygen as auxiliary atoms. Optimization of this approach resulted in an atomically reconstructed copper electrode (denoted as Cu-50) with a surface tensile strain of 1.1% and preferential exposure of Cu(100) facets. Cu-50 delivered remarkable Faradaic efficiencies (up to 72%) for C_{2+} products during CER, with a 53% selectivity for ethylene (10-fold higher than for a non-reconstructed Cu foil). This work guides the design of advanced copper-based catalysts that promote C–C coupling, demonstrating the potential of tailored copper structures for efficient conversion of CO_2 to valuable C_{2+} products.

Keywords CO_2 electroreduction, atom reconfiguration, copper, C–C coupling, ethylene

1 Introduction

CO_2 electroreduction (CER) offers a promising pathway for the conversion of carbon dioxide into valuable chemicals and fuels, thereby storing renewable energy as chemical bonds while mitigating environmental impacts [1–3]. While significant experimental progress has been made recently relating to the selective synthesis of single-carbon (C_1) products such as CO, CH_4 and formate, the energy-efficient and selective synthesis of multi-carbon (C_{2+}) compounds like ethylene, propylene, ethanol, or propanol remains a formidable challenge in CER [4–6].

According to the Sabatier principle, the adsorption energies of different carbon intermediates involved in multi-step reactions scale with one another [7]. At the atomic level, copper, is recognized as the only metal capable of reducing CO_2 to complex hydrocarbons and oxygenates [5,8]. However, the moderate binding energies of most reaction intermediates on copper surfaces enable various reaction pathways to occur simultaneously, meaning CER over copper catalysts inevitably yields multiple products [9]. Thus, enhancing the Faradaic efficiency (FE) of single-product formation in CER is the prized goal of current research. The critical step for generating C_{2+} products is the C−C coupling process, which is highly sensitive to the catalyst's surface structure [1,10,11]. It has been found that surface atomic engineering (e.g., heteroatom-doping) [12–15] and interface atomic or molecular engineering (e.g., interfacial bonding) [16–18], which can induce neighboring metal atoms with a different charge compared to their pristine state, can induce novel physicochemical properties and strong synergistic effects for electrocatalysts. Interface engineering through various routes like chemical doping and post-treatment utilizes weak (e.g., hydrogen bonding, electrostatic attraction, van der Waals interaction) or strong (e.g., covalent bonding) coupling effects. Such effects not only induce changes to the local coordination

Received November 19, 2024; accepted November 28, 2024;
online February 23, 2025

E-mails: kuangy@tsinghua-sz.edu.cn (Kuang Y),
zhoudj@buct.edu.cn (Zhou D),
sunxm08@126.com (Sun X)

environment and electronic states of metal surfaces but also allow separate reaction processes to occur in close proximity at different active sites to collaboratively expedite catalysis [19,20]. Accordingly, atomic-level manipulation of the crystallinity and structure of active metal surfaces (e.g., introducing strain) [2,21] in hybrid systems is a promising strategy for the design of advanced catalysts with broad electrocatalytic applications. However, how to properly facilitate the surface reconstruction of metal surfaces, like copper, to boost activity and product selectivity remains elusive.

Herein, using easy-to-regulate electrochemical synthesis techniques, we described a new method for reconstructing Cu surfaces for improved CER to ethylene. Briefly, the surface oxidation of a copper foil in the presence of NaOH, Na_2S, or lactic acid led to the formation of surface Cu_2O, Cu_2S, and $[CuL_2(OH)]^{3-}$ species, which in turn were electrochemically reduced to form reconstructed copper surfaces preferentially exposing Cu(100) facets and possessing significant tensile strain (1.1%). The reconstructed copper electrodes delivered a remarkable FE of up to 72% for C_{2+} products during CER, with an impressive 53% selectivity for ethylene. This study introduces a simple synthetic pathway toward advanced Cu-based electrocatalysts for converting CO_2 into ethylene.

2 Material and methods

2.1 Materials and chemicals

All reagents were obtained from commercial suppliers and used as received without further purification. L-lactic acid (⩾ 85%), NaOH (⩾ 95%, granular), KCl (⩾ 99.99%) and KOH (⩾ 99.99%) were purchased from Shanghai Macklin Biochemical Co., Ltd. Na_2S (99%) was purchased from Sigma-Aldrich. Cu foil (⩾ 99.999%) was purchased from Alfa Aesar. Deionized water with a resistivity ⩾ 18 mΩ was used to prepare all aqueous solutions.

2.2 Synthesis of copper catalysts

Under ice bath conditions, 400 mL of deionized water was added to a beaker, followed by the introduction of 2.3 $mol\cdot L^{-1}$ lactic acid, 3.2 $mol\cdot L^{-1}$ KOH, and a certain amount of Na_2S. A carbon rod, a saturated calomel electrode, and a copper foil (with an immersed area of 1 cm × 1 cm in the electrolyte) were used as the counter electrode, reference electrode, and working electrode, respectively. Cyclic voltammetry (CV) was then utilized to perform a specific number of scans within a predetermined potential range. At a Na_2S concentration of 5 $mmol\cdot L^{-1}$, samples derived from 15, 50, 75 CV cycles ranging from −1.55 to −0.9 V_{SCE} followed by a subsequent 5-min CER test were designated as Cu-15, Cu-50, and Cu-75, respectively. At a Na_2S concentration of 0 $mmol\cdot L^{-1}$, the sample derived from 50 CV cycles ranging from −1.55 to −0.3 V_{SCE} followed by a subsequent 5-min CER test was designated as 0-Cu-50. At a Na_2S concentration of 10 $mmol\cdot L^{-1}$, the sample derived from 50 CV cycles ranging from −1.55 to −0.9 V_{SCE} followed by a subsequent 5-min CER test was designated as 10-Cu-50.

2.3 Physical characterizations

Scanning electron microscopy (SEM) images were obtained on a Zeiss Supra 55 scanning electron microscope operating at 10 kV, and the corresponding energy dispersive spectroscopy (EDS) elemental mappings were performed using an energy-dispersive spectrometer. High resolution transmission electron microscopy (HRTEM) images were collected on a JEOL JEM-2100 HRTEM operating at an accelerating voltage 200 kV. X-ray diffraction (XRD) patterns were collected on a Bruker D8 Advance X-ray powder diffractometer equipped with a Cu Kα radiation source (λ = 0.15405 nm) operating at 40 kV. Diffraction data were collected in a 2θ range from 10° to 90° at a scanning rate of $5^\circ\cdot min^{-1}$. X-ray photoelectron spectroscopy (XPS) was conducted on a Shimadzu Kratos Analytical AXIS Supra equipped with an Al Kα X-ray source (1486.6 eV). All binding energies were calibrated using the C 1s carbon peak (284.8 eV) of adventitious hydrocarbons. Raman spectra were recorded on a HORIBA LabRAM Aramis equipped with a 532 nm laser. Inductively coupled plasma (ICP)-optical emission spectrometry and ICP-mass spectrometry analyses were carried out on a Thermo Fisher iCAP 7400.

2.4 Electrochemical measurements

CER electrochemical measurements were performed in a standard three-electrode system at room temperature (25 °C) on an electrochemical workstation (CorrTest CS2350H), using the copper catalysts as the working electrodes, a graphite rod as the counter electrode and a Ag/AgCl electrode as the reference electrode. The catholyte was 0.1 $mol\cdot L^{-1}$ KCl, and the anolyte was CO_2-saturated 0.1 $mol\cdot L^{-1}$ $KHCO_3$.

3 Results and discussion

We developed a facile *in situ* CV electrochemical sulfidation and reduction strategy to reconstruct the copper surface with the assistance of lactic acid, which transformed the surface of Cu foil into a uniform thin layer of Cu_2O/Cu_2S phases nanoparticles. As shown in Fig. 1(a),

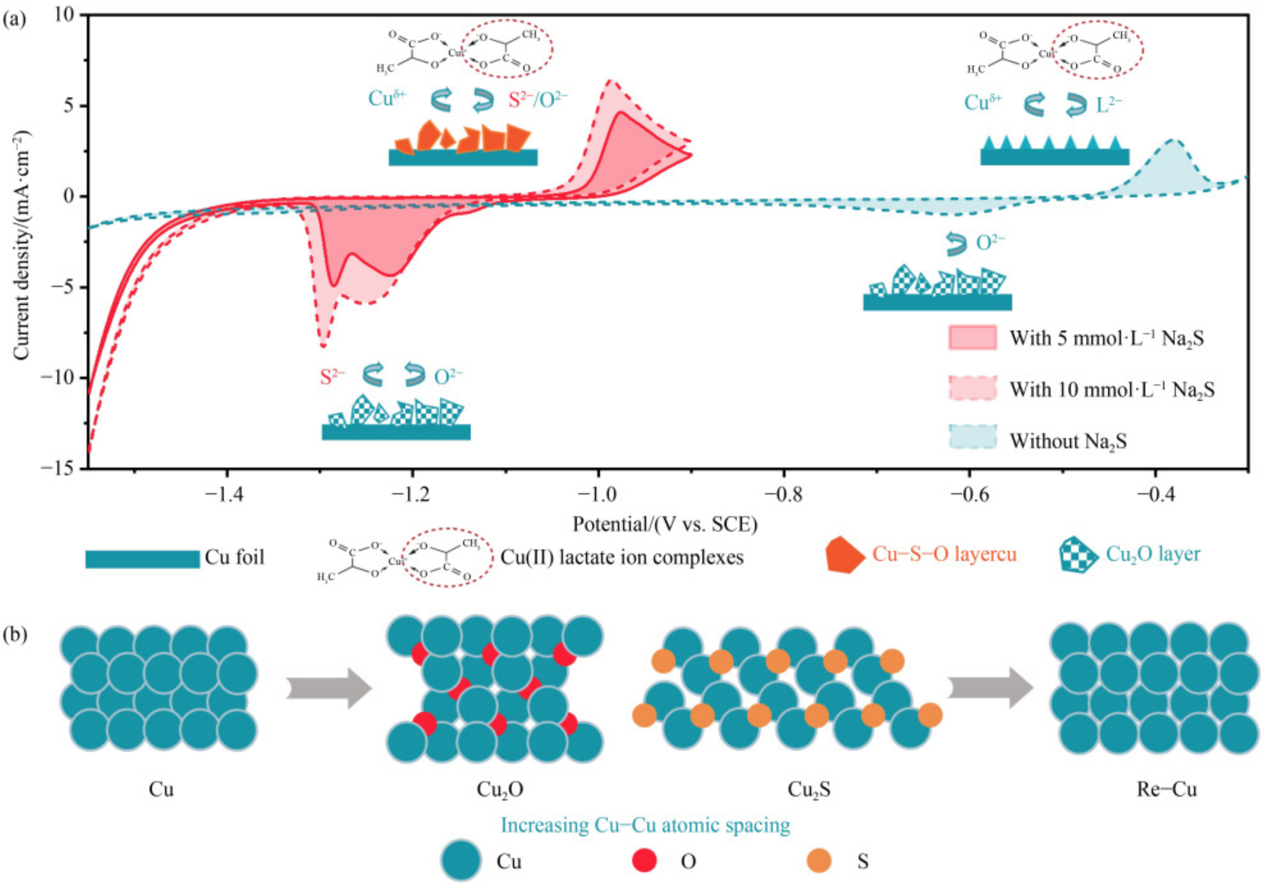

Fig. 1 Cyclic voltammograms showing the formation of $Cu_{2-x}S$ and Cu_2O nanoparticles on the surface of a copper foil. (a) CV method for the synthesis of Cu_2O/Cu_2S phases nanoparticles on Cu foils. Representative CV curves from −1.55 to −0.9 V_{SCE} in electrolytes containing 2.3 $mol \cdot L^{-1}$ lactic acid, 3.2 $mol \cdot L^{-1}$ NaOH (pH = 13) with or without Na_2S at room temperature; (b) structural comparison of Cu, Cu_2O, Cu_2S, and reconstructed Cu possessing significant tensile stress.

an oxidation peak was observed around −0.9 V_{SCE}, while two reduction peaks were seen in the range from −1.2 to −1.4 V_{SCE}. The peak at −0.9 V_{SCE} represents the oxidation of Cu_2S [22]. With an increase of the Na_2S concentration, the area of this oxidation peak increased, accompanied by a negative shift of the oxidation peak position. This demonstrated that the copper foil surface could sulfurized to Cu_2S in the presence of Na_2S. During the reverse scan, two distinct reduction peaks were observed. In alkaline electrolytes containing sodium lactate, lactate ions (L^{2-}) are hydrolyzed to generate OH^-. When the applied potential reaches the standard potential of the $E_{Cu^+/Cu}$ and $E_{Cu^{2+}/Cu}$ redox couples, the Cu^+ and Cu^{2+} ions will dissolve from the copper electrode. At this point, Cu^+ interacts with OH^-, S^{2-}, and L^{2-}, respectively, to produce Cu_2O, Cu_2S, and $[CuL_2(OH)]^{3-}$ (Cu^{2+} and lactic acid ions initially form $CuL_2{}^{2-}$, which further reacts with OH^- in the electrolyte to produce the $[CuL_2(OH)]^{3-}$ [23]). Therefore, the two reduction peaks seen in the CV curves during the reduction sweep represent the reduction of Cu_2O or Cu_2S and the electroprecipitation of the $[CuL_2(OH)]^{3-}$ on the electrode surface, respectively. The hydrogen evolution reaction (HER) reaction dominates below −1.4 V_{SCE}. Conversely, in the absence of Na_2S, copper oxidation peaks appear below −0.40 V_{SCE}, and corresponding reduction peaks appear at −0.65 V_{SCE}, due to the formation of Cu_2O and the *in situ* reduction to form metallic copper, respectively. For Cu(100) surfaces, the Cu–Cu spacings for metallic Cu, Cu_2O and Cu_2S are 2.56 Å, 3.01 Å and 3.93 Å, respectively. As a result, the Cu–Cu spacing will change significantly upon conversion of Cu to Cu_2O or Cu_2S (Fig. 1(b)), while introducing significant strain when the surface Cu_2O and Cu_2S are reduced back to metallic Cu.

On the basis of the above, we conducted a thorough investigation of the influence of CV scan cycles, potential scan range and Na_2S concentration on the structural characteristics of our modified copper electrodes and subsequently the CER performance of our samples. At a 5 $mmol \cdot L^{-1}$ Na_2S concentration, the samples obtained following 15, 50, and 75 cycles of CV scans followed by a subsequent 5-min CER test were designated as Cu-15, Cu-50, and Cu-75, respectively. At Na_2S concentrations of 0 and 10 $mmol \cdot L^{-1}$, the samples derived from 50 CV cycles followed by a subsequent 5-min CER test were labeled as 0-Cu-50 and 10-Cu-50, respectively.

As revealed by SEM, the surface of the original Cu foil was smooth (Fig. 2(a)). HRTEM analysis shows a

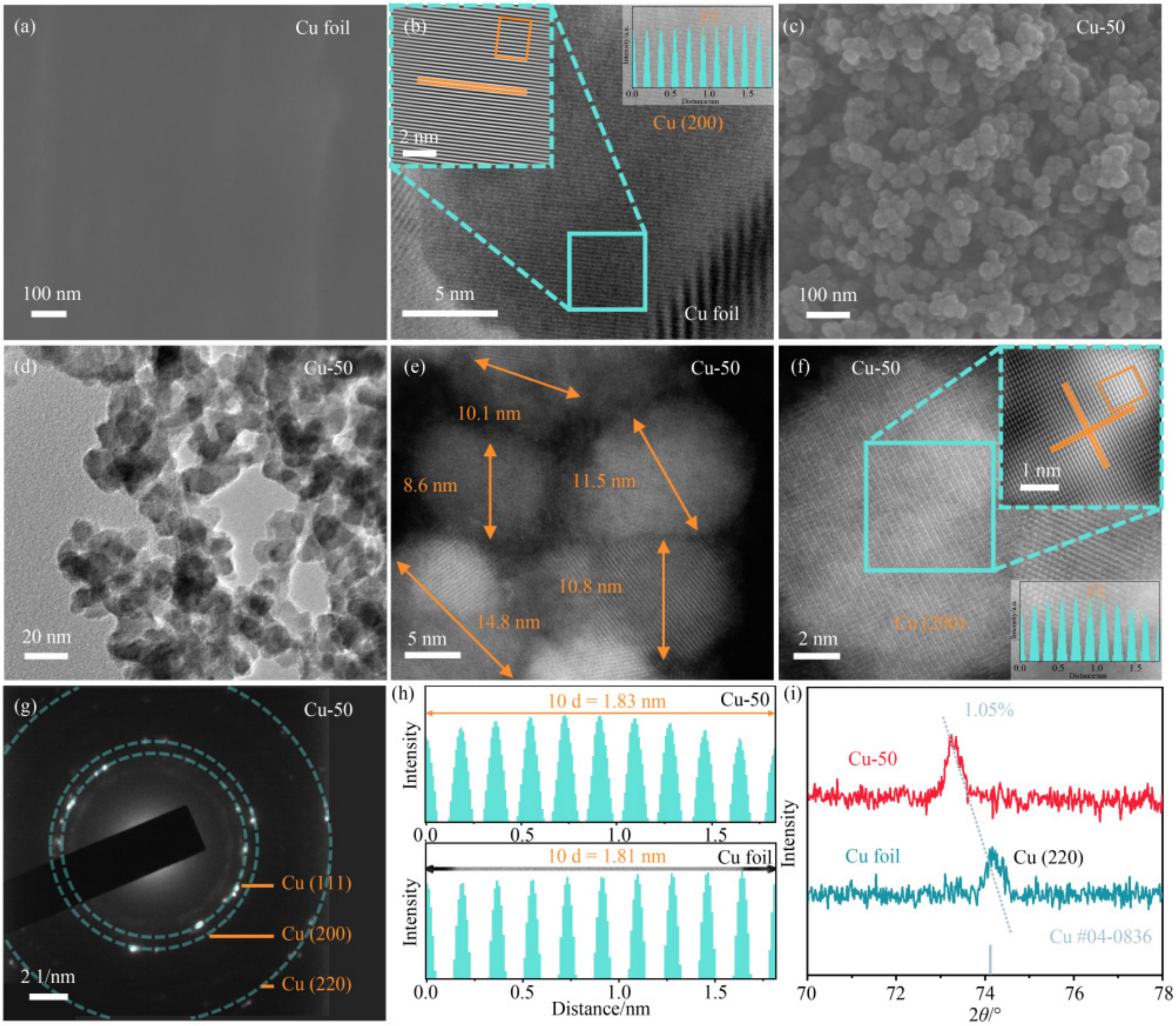

Fig. 2 Morphological and structural characterizations of the Cu foil and Cu-50. (a) SEM image, and (b) HRTEM image of Cu foil; (c) SEM image, (d) HRTEM image, and (e, f) HAADF-STEM images of Cu-50; (g) corresponding SAED image of Cu-50; (h) comparison of lattice fringe spacings for Cu foil and Cu-50; (i) XRD patterns of Cu foil and Cu-50.

lattice fringe with a spacing of 0.181 nm on the Cu foil (Fig. 2(b)), corresponding to the Cu(200) facets of face-centered cubic (FCC) Cu. In contrast, irregular nanoparticles with a size of 10–15 nm were observed on the surface of the Cu foil after the electrooxidation-reduction treatment (Figs. 2(c)–2(e)). HRTEM analysis reveals lattice fringes with a spacing of 0.183 nm for Cu-50 (Fig. 2(f)), corresponding to the Cu(200) facets of FCC Cu. Furthermore, the selected-area electron diffraction (SAED) pattern for Cu-50 shown in Fig. 2(g) displayed a series of distinct diffraction rings associated with the Cu(111), Cu(200), and Cu(220) facets of metallic Cu. The corresponding EDS-mapping element distribution images also confirmed that the surface of Cu-50 was composed of copper particles (Fig. S1, cf. Electronic Supplementary Material, ESM). Comparing the lattice fringe spacings of the Cu(200) facets for Cu foil and Cu-50 (Fig. 2(h)), the lattice spacing of the Cu foil matches that of standard bulk copper (0.181 nm), whereas the lattice spacing of Cu-50 is notably increased (0.183 nm), indicating the presence of a 1.1% tensile strain on the Cu(200) facet of Cu-50. Further characterization of the phase composition and crystal structure was conducted using XRD. As shown in Fig. S2 (cf. ESM) and Fig. 2(i), the XRD patterns of Cu foil and Cu-50 exhibit primary peaks that correspond to Cu (JCPDS No. 04-0836). The intense diffraction peak at 50.4° is assigned to the Cu(200) plane. Since the reconstruction is confined to the surface, with the diffraction peak corresponding to the Cu(200) plane being very intense, no peak shift associated with lattice strain was seen in the Cu(200) peak for Cu-50. However, the weaker Cu (220) peak in XRD pattern for Cu-50 was shifted by 0.9° to a lower angle relative to the Cu foil. This shift, in accordance with Bragg's law, indicates a 1.05% tensile strain in the lattice of surface copper atoms in Cu-50 [2,21,24]. These findings confirm that the interatomic spacing of copper on the catalyst surface has been modulated by the presence of sulfur and oxygen as auxiliary atoms during the catalyst synthesis.

As shown in Fig. S12 and Table S1 (cf. ESM), the structure of the Cu-50 catalyst was characterized after synthesis and before undergoing CER testing. Besides, the XPS data indicated that the sample contained trace amounts of oxygen and sulfur elements (Figure S13, cf. ESM). Additionally, the morphologies of Cu-15 and Cu-75, which underwent different numbers of CV cycles compared to Cu-50, were depicted in Figs. S3 and S4 (cf. ESM), respectively. As the number of CV cycles increased, the surface of the copper foil became progressively rougher. As shown in Fig. S14 (cf. ESM), both Cu-15 and Cu-75 exhibited lattice strain in the Cu(200) planes. However, the degree of strain varied between the two catalysts. With increasing electrochemical oxidation-reduction rates, the lattice strain in the Cu(200) planes of the copper-based catalyst surfaces increased. The morphologies of 0-Cu-50 and 10-Cu-75, obtained by altering the concentration of Na_2S in the synthesis solution, are shown in Figs. S5 and S6 (cf. ESM), respectively. With an increase in sulfur ion concentration in the solution, the particle shape on the catalyst surface changed from spheroidal at low concentrations to flake-like particles at a 10 $mmol \cdot L^{-1}$ sulfur ion concentration.

Next, laser Raman spectroscopy was utilized to elucidate the structural and phase composition on the surface of the catalysts. The Raman spectra of catalysts were recorded in the range of 100–1000 cm^{-1} (Fig. 3(a)). Atmospheric oxygen induces partial oxidation in copper-based electrodes, resulting in the appearance of Cu–O vibrational peaks. Peaks at 285 cm^{-1} (A_{1g}), 335 cm^{-1} (B_{1g}), and 620 cm^{-1} (B_{2g}) confirm the presence of surface CuO [25,26]. Additionally, peaks observed at 150 cm^{-1} (phonon symmetry $\Gamma^{-}{}_{15}$) [27], 217 cm^{-1} (second-order Raman mode ${}^{2}\Gamma^{-}{}_{12}$) [28], 410 cm^{-1} (four-phonon mode ${}^{3}\Gamma^{-}{}_{12} + \Gamma^{-}{}_{25}$) [28] and 632 cm^{-1} (infrared-allowed mode) [29] confirm the presence of the Cu_2O phase [30,31]. The Raman spectra indicate that the Cu foil tends to oxidize into CuO after a 5-min CER test. Furthermore, copper surfaces with tensile stress showed less CuO but an increasing fraction of Cu_2O as the number of CV cycles increased, indicating a tendency for strained Cu to oxidize into the more stable Cu_2O. As a result, the surface of the treated Cu foils gradually become covered by polycrystalline Cu_2O nanoparticles without any preferential orientation with increasing CV cycles.

XPS was utilized to investigate the chemical composition and oxidation states of the copper surface for both the Cu foil and Cu-50. The Cu $2p_{3/2}$ spectra are deconvoluted into two peaks at 935.2 and 932.5 eV, corresponding to Cu^{2+} and Cu^{+}/Cu^{0}, respectively (Fig. 3(b)) [8]. In the two peaks of Cu $2p_{2/3}$, the area percentage of $Cu^{0/+}$ for Cu foil and Cu-50 are 84.2% and 91.3%, respectively (Table S2, cf. ESM). The spectrum of the Cu foil showed a higher percentage of Cu^{2+} compared to Cu-50. Due to the 0.1 eV difference in binding energies between Cu^{+} and Cu^{0}, these oxidation states are indistinguishable in the Cu 2p region. Consequently, we also acquired X-ray excited Auger electron spectra (AES) from the Cu LMM region (Fig. 3(c)), which clearly indicated that Cu-50 contained a greater proportion of Cu^{+} (569.9 eV) than Cu^{0} (568.0 eV) [32,33], while near surface region of the Cu foil was dominated by Cu^{0}. In the two peaks of Cu LMM, the area percentage of Cu^{0} for Cu foil and Cu-50 are 65.4% and 32.2%, respectively (Table S3, cf. ESM). This further confirms that after a 5-min CER test, the Cu foil tended to oxidize into CuO, whereas Cu-50 tended to oxidize into Cu_2O, consistent with the Raman results. In addition, the S 2p XPS spectra confirmed the absence of sulfur in both the Cu foil and Cu-50 samples (Fig. S7, cf. ESM).

The CER performance of restructured copper catalysts was initially assessed using a three-electrode setup. Linear sweep voltammetry (LSV) was carried out in 0.1 $mol \cdot L^{-1}$ KCl saturated with N_2/CO_2 to evaluate the electrochemical activity. It is evident that the Cu-50 displayed a higher current density compared to Cu foil (Fig. 4(a)). Furthermore, Cu-50 exhibited the highest current densities relative to other synthesized samples

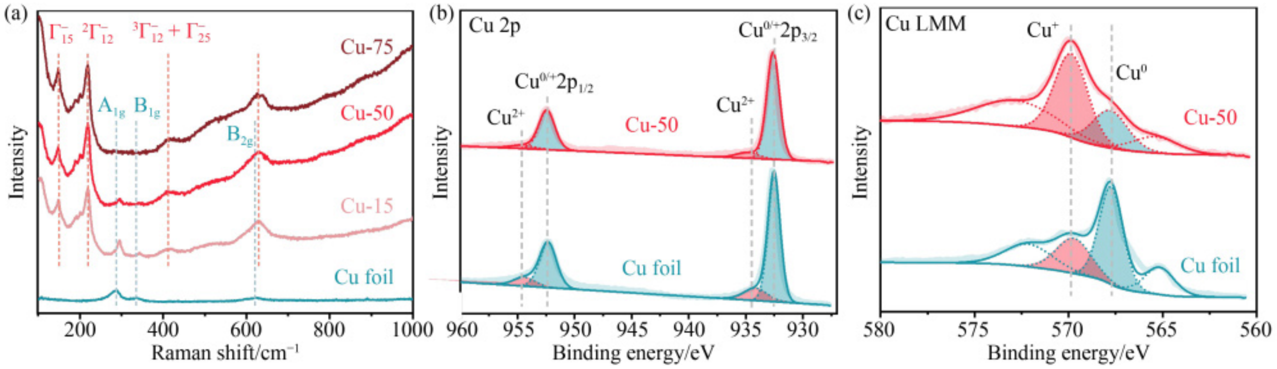

Fig. 3 Surface structural characterization of the Cu foil and Cu-50. (a) Raman spectra of Cu foil, Cu-15, Cu-50, and Cu-75; (b) Cu 2p XPS spectra of Cu foil and Cu-50; (c) AES of Cu LMM of Cu foil and Cu-50.

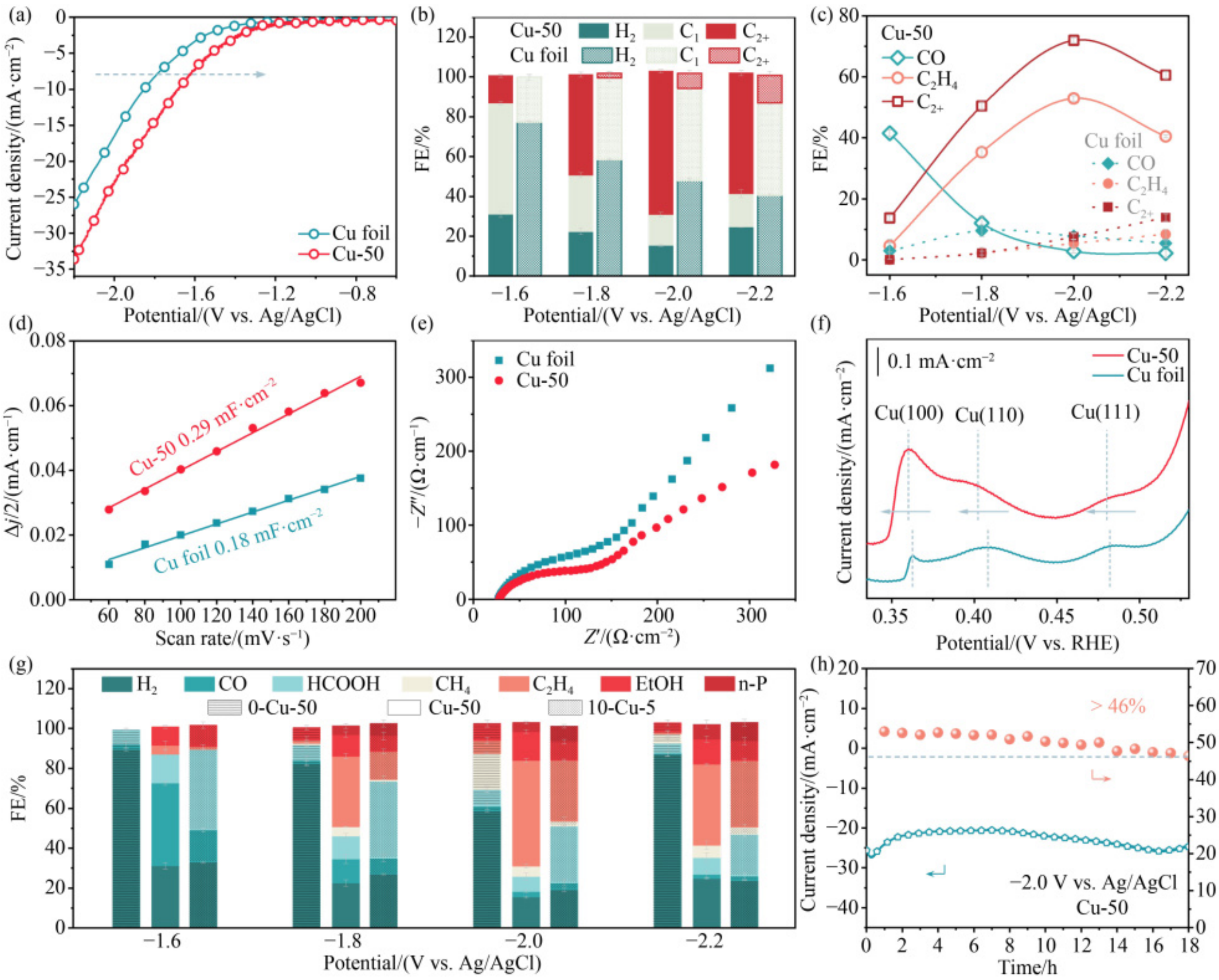

Fig. 4 CER performance of restructured Cu cathodes. (a) LSV curves of Cu foil and CV-50 at a scanning rate of 5 mV·s^{-1} in the CO_2-saturated 0.1 mol·L^{-1} KCl aqueous solution; (b) FE of C_{2+}, C_1 and H_2 products of Cu foil and CV-50; (c) comparison of the FE of C_2H_4, C_{2+} and CO on Cu foil and CV-50; (d) determination of the C_{dl} of Cu foil and CV-50, used for estimating the ECSA; (e) Nyquist plots of Cu foil and CV-50 at OCP; (f) LSV curves in Ar-saturated 1 mol·L^{-1} KOH of Cu foil and CV-50 at the scan rates of 50 mV·s^{-1}; (g) Faradaic efficiencies of all products during CER on 0-Cu-50, Cu-50 and 10-Cu-50; (h) stability test of Cu-50 at −2.0 $V_{Ag/AgCl}$.

(Fig. S8, cf. ESM). The Cu-50 with electrooxidation-reduction mediated by sulfur and oxygen atoms, delivered a decreased overpotential and a higher total current density compared to all the other catalysts, indicating its enhanced electrochemical activity. The FE of all products for the various Cu cathodes are depicted in Figs. S9 and S10 (cf. ESM). The copper foil showed significant hydrogen evolution and high selectivity for C_1 products, consequently offering low selectivity for C_{2+} products. However, the selectivity toward C_{2+} products was notably enhanced in copper catalysts that had undergone electrochemical restructuring. The $FE_{C_{2+}}$ of Cu-50 at −2.0 $V_{Ag/AgCl}$ reached up to 72%, which is 9 times that of the Cu foil, suggesting a positive relationship between tensile stain at the Cu surface and enhanced C–C coupling. Along with a high $FE_{C_{2+}}$, Cu-50 showed suppressed HER conversion (15% at −2.0 $V_{Ag/AgCl}$) compared to the Cu foil (Fig. 4(b)). In the copper-catalyzed CER process, it is widely accepted that CO_2 is initially reduced to *CO. Subsequently, at a higher overpotential, the adsorbed *CO undergoes C–C coupling reactions to form C_{2+} products [1,34]. The adsorption of the intermediate *CO and the subsequent C–C coupling are pivotal steps that determine the catalyst's ability to reduce carbon dioxide to ethylene [35–37]. Thus, there is a correlation between CO production and the formation of C_{2+} products. As illustrated in Fig. 4(c), FE_{CO} of Cu-50 gradually decreased with a negative potential shift. In contrast, the FE for ethylene and C_{2+} products were concurrently enhanced. $FE_{C_2H_4}$ of Cu-50 reaches its maximum of 53% at −2.0 $V_{Ag/AgCl}$, which was 10 times that of the Cu foil at the same potential. The presence of tensile stress in the Cu-50 catalyst thus appeared important for modulating the adsorption strength of CER intermediates, thereby promoting C–C coupling during CER [2,38] and resulting in a very high selectivity for ethylene.

The electrochemically active surface area (ECSA) of each catalyst was estimated from the double-layer capacitance (C_{dl}) obtained via CV tests at different scan rates. Cu-50 exhibited a larger C_{dl} of 0.29 $mF \cdot cm^{-2}$ compared to the Cu foil (0.18 $mF \cdot cm^{-2}$), implying more highly exposed active sites in Cu-50 (Fig. 4(d) and Fig. S11 (cf. ESM)). Cu-50 also displayed a smaller semicircular arc in the Nyquist plot compared to Cu foil, indicating that Cu-50 catalyst exhibited faster charge transfer kinetics (Fig. 4(e)).

To probe the link between structure and performance in the various catalysts, we investigated the reactivity of the Cu(100) facets, which are widely acknowledged for their robust C – C coupling activity. We utilized the electro-sorption of hydroxide (OH_{ad}) to probe the surface structure as per previous studies, where distinct Cu facets exhibit unique OH_{ad} peaks in the LSV curves [39,40]. LSV measurements of OH^- adsorption were performed in an Ar-saturated 1 $mol \cdot L^{-1}$ KOH solution, scanning from 0.3 to 0.55 V_{RHE} at a rate of 50 $mV \cdot s^{-1}$. As shown in Fig. 4(f), Cu-50 exhibited a lower Cu(100) oxidation potential and a more pronounced Cu(100) oxidation peak. This alteration can be attributed to enhanced *CO adsorption on the Cu-50 catalyst surface due to lattice tensile stress, aligning with our experimental findings on tensile stress effects in promoting C–C coupling.

Additionally, we modulated the concentration of sulfur ions in the catalyst synthesis solution, and then tested the CER performance of the different catalysts. The 0-Cu-50 catalyst synthesized in the absence of sulfur ions demonstrated high HER activity, confirming that the auxiliary element sulfur is indispensable for regulating the Cu structure to enhance CER. In contrast, the 10-Cu-50 catalyst synthesized under high sulfur ion concentrations exhibited a higher selectivity for the formate, resulting in lower selectivity for C_{2+} products compared to Cu-50 (Fig. 4(g)). These results indicate that the sulfur ion concentration during synthesis plays a significant role in the CER activity of the final catalyst. Furthermore, the number of CV cycles during the synthesis process also impacted catalyst selectivity. As shown in Figs. S10(b)–10(d), Cu-15 (fewer CV cycles compared to Cu-50) had a relatively low coverage of nanoparticles on the copper foil surface (Fig. S3). The structure of this catalyst was less conducive to C–C coupling, resulting in higher selectivity for H_2 and C_1 products. In contrast, Cu-75 (more CV cycles compared to Cu-50) showed an increased coverage of nanoparticles on the copper foil surface, with the surface being entirely covered by irregular nanoparticles (Fig. S4). At −2.0 $V_{Ag/AgCl}$, the $FE_{C_{2+}}$ exceeds 50%, but due to slightly higher FE for HER and C_1 products, the selectivity for C_{2+} was lower than that of Cu-50.

As shown in Fig. 4(h), Cu-50 exhibits the capability to sustain stable electrolysis for more than 18 h at −2.0 $V_{Ag/AgCl}$, while maintaining a high FE of over 46% for the production of C_2H_4, thereby validating the catalyst's durability.

4 Conclusions

We have discovered a simple synthetic route toward copper-based catalysts possessing significant surface tensile strain and a preferential Cu(100) orientation. By optimizing the tensile strain, impressive C–C coupling during CER can be achieved, evidenced by a 72% FE for C_{2+} products and a 53% selectivity for ethylene at −2.0 $V_{Ag/AgCl}$, outperforming a pristine Cu foil by a factor of ten in terms of $FE_{C_2H_4}$ with good suppression of HER. This work underscores the potential of surface and interface engineering in modulating catalyst performance for CER, paving the way for the design of efficient electrocatalysts for the selective conversion of CO_2 into high-value C_{2+} compounds.

Acknowledgements This work was financially supported by the National Key Research and Development Program of China (Grant No. 2021YFA-1502200), the Shenzhen Science and Technology Program (Nos. RCJC2023-1211090051085, KJZD20230923115759014, JCYJ20230807151159002), the National Natural Science Foundation of China (Grant No. 21935001, 22175012), the National Key Beijing Natural Science Foundation (Grant No. Z210016), the Young Elite Scientists Sponsorship Program by CAST (No. 2022QNRC001), the Project of PetroChina Technology Management Department (No. 2023ZZ1202), and the long-term subsidy mechanism from the Ministry of Finance and the Ministry of Education of China. GINW acknowledges funding support from the MacDiarmid Institute for Advanced Materials and Nanotechnology.

Electronic Supplementary Material Supplementary material is available in the online version of this article at http://doi.org/10.1007/s11705-025-2527-4 and is accessible for authorized users.

Competing interests The authors declare that they have no competing interests.

References

1. Gao D, Arán-Ais R M, Jeon H S, Roldan Cuenya B. Rational catalyst and electrolyte design for CO_2 electroreduction towards multicarbon products. Nature Catalysis, 2019, 2(3): 198–210
2. Lei Q, Huang L, Yin J, Davaasuren B, Yuan Y, Dong X, Wu Z P, Wang X, Yao K X, Lu X, et al. Structural evolution and strain generation of derived-Cu catalysts during CO_2 electroreduction. Nature Communications, 2022, 13(1): 4857
3. Wu H, Li J, Qi K, Zhang Y, Petit E, Wang W, Flaud V, Onofrio N, Rebiere B, Huang L, et al. Improved electrochemical conversion of CO_2 to multicarbon products by using molecular doping. Nature Communications, 2021, 12(1): 7210
4. Chang B, Pang H, Raziq F, Wang S, Huang K W, Ye J, Zhang H. Electrochemical reduction of carbon dioxide to multicarbon (C_{2+})

products: challenges and perspectives. Energy & Environmental Science, 2023, 16(11): 4714–4758

5. Chen J, Qiu H, Zhao Y, Yang H, Fan L, Liu Z, Xi S, Zheng G, Chen J, Chen L, et al. Selective and stable CO_2 electroreduction at high rates via control of local H_2O/CO_2 ratio. Nature Communications, 2024, 15(1): 5893
6. Wang H, Sun R, Liu P, Hu H, Ling C, Han X, Shi Y, Zheng X, Wu G, Hong X. Interstitial carbon induces enriched $Cu^{\delta+}$ sites in Cu_2O nanoparticles to facilitate CO_2 electroreduction to C_{2+} products. Nano Research, 2024, 17(8): 7013–7019
7. Sabatier P. Catalysis in Organic Chemistry. Paris: Librairie Polytechnique, Ch. Beranger, 1920, Vol. 3
8. Deng H, Liu T, Zhao W, Wang J, Zhang Y, Zhang S, Yang Y, Yang C, Teng W, Chen Z, et al. Substituent tuning of Cu coordination polymers enables carbon-efficient CO_2 electroreduction to multi-carbon products. Nature Communications, 2024, 15(1): 9706
9. Bagger A, Ju W, Varela A S, Strasser P, Rossmeisl J. Electrochemical CO_2 reduction: a classification problem. ChemPhysChem, 2017, 18(22): 3266–3273
10. Arán-Ais R M, Gao D, Roldan Cuenya B. Structure-and electrolyte-sensitivity in CO_2 electroreduction. Accounts of Chemical Research, 2018, 51(11): 2906–2917
11. Lian Z, Dattila F, López N. Stability and lifetime of diffusion-trapped oxygen in oxide-derived copper CO_2 reduction electrocatalysts. Nature Catalysis, 2024, 7(4): 401–411
12. You S, Xiao J, Liang S, Xie W, Zhang T, Li M, Zhong Z, Wang Q, He H. Doping engineering of Cu-based catalysts for electrocatalytic CO_2 reduction to multi-carbon products. Energy & Environmental Science, 2024, 17(16): 5795–5818
13. Xie Y, Ou P, Wang X, Xu Z, Li Y C, Wang Z, Huang J E, Wicks J, McCallum C, Wang N, et al. High carbon utilization in CO_2 reduction to multi-carbon products in acidic media. Nature Catalysis, 2022, 5(6): 564–570
14. Li X, Qin M, Wu X, Lv X, Wang J, Wang Y, Wu H B. Enhanced CO affinity on Cu facilitates CO_2 electroreduction toward multi-carbon products. Small, 2023, 19(39): 2302530
15. Li P, Bi J, Liu J, Wang Y, Kang X, Sun X, Zhang J, Liu Z, Zhu Q, Han B. p–d Orbital hybridization induced by p-block metal-doped Cu promotes the formation of C_{2+} products in ampere-level CO_2 electroreduction. Journal of the American Chemical Society, 2023, 145(8): 4675–4682
16. Xiong W F, Si D H, Li H F, Song X, Wang T, Huang Y B, Liu T F, Zhang T, Cao R. Steering CO_2 electroreduction selectivity U-turn to ethylene by Cu–Si bonded interface. Journal of the American Chemical Society, 2024, 146(1): 289–297
17. Liu Y, Gong L, Liu J, Xiao P, Chen B, Xie F, Yang C, Wu Z. Fabrication of interface with capping-bonding synergy to boost CO_2 electroreduction to formate. Applied Catalysis B: Environment and Energy, 2025, 362: 124760
18. Ren S, Cao X, Fan Q, Yang Z, Wang F, Wang X, Bai L, Yang J. Selective CO_2 electroreduction to multi-carbon products on organic-functionalized CuO nanoparticles by local micro-environment modulation. Nano-Micro Letters, 2024, 16(1): 262
19. Stamenkovic V R, Strmcnik D, Lopes P P, Markovic N M. Energy and fuels from electrochemical interfaces. Nature Materials, 2017, 16(1): 57–69
20. Subbaraman R, Tripkovic D, Strmcnik D, Chang K C, Uchimura M, Paulikas A P, Stamenkovic V, Markovic N M. Enhancing hydrogen evolution activity in water splitting by tailoring Li^+-$Ni(OH)_2$-Pt interfaces. Science, 2011, 334(6060): 1256–1260
21. Li S, Wu G, Mao J, Chen A, Liu X, Zeng J, Wei Y, Wang J, Zhu H, Xia J. Tensile-strained Cu penetration electrode boosts asymmetric C−C coupling for ampere-level CO_2-to-C_{2+} reduction in acid. Angewandte Chemie International Edition, 2024, 63(41): e202407612
22. Vasquez Moll D, De Chialvo M R G, Salvarezza R C, Arvia A J. Corrosion and passivity of copper in solutions containing sodium sulphide. Analysis of potentiostatic current transients. Electrochimica Acta, 1985, 30(8): 1011–1016
23. Chen T, Kitada A, Seki Y, Fukami K, Usmanov D T, Chen L C, Hiraoka K, Murase K. Identification of copper(II)–lactate complexes in Cu_2O electrodeposition baths: deprotonation of the α-hydroxyl group in highly concentrated alkaline solution. Journal of the Electrochemical Society, 2018, 165(10): D444–D451
24. Wang H, Zhang H, Huang Y, Wang H, Ozden A, Yao K, Li H, Guo Q, Liu Y, Vomiero A, et al. Strain in copper/ceria heterostructure promotes electrosynthesis of multicarbon products. ACS Nano, 2023, 17(1): 346–354
25. Zoolfakar A S, Rani R A, Morfa A J, O'Mullane A P, Kalantar-Zadeh K. Nanostructured copper oxide semiconductors: a perspective on materials, synthesis methods and applications. Journal of Materials Chemistry C, 2014, 2(27): 5247–5270
26. Kudryashov D, Monastyrenko A, Mozharov A, Bukatin A, Nikitina E, Pirogov E, Gudovskikh A. Copper(I) oxide rf-magnetron sputtering at elevated substrate temperatures. Journal of Physics: Conference Series, 2017, 917(3): 032020
27. Compaan A, Cummins H. Resonant quadrupole-dipole Raman scattering at the 1s yellow exciton in Cu_2O. Physical Review Letters, 1973, 31(1): 41–44
28. Yu P Y, Shen Y R. Resonance Raman studies in Cu_2O. I. The phonon-assisted 1s yellow excitonic absorption edge. Physical Review B: Solid State, 1975, 12(4): 1377–1394
29. Powell D, Compaan A, Macdonald J, Forman R. Raman-scattering study of ion-implantation-produced damage in Cu_2O. Physical Review B: Solid State, 1975, 12(1): 20–25
30. Wu M K, Ashburn J R, Torng C J, Hor P H, Meng R L, Gao L, Huang Z L, Wang Y Q, Chu C W. Superconductivity at 93 K in a new mixed-phase Y-Ba-Cu-O compound system at ambient pressure. Physical Review Letters, 1987, 58(9): 908–910
31. Ravichandiran C, Sakthivelu A, Deva Arun Kumar K, Davidprabu R, Valanarasu S, Kathalingam A, Ganesh V, Shkir M, Algarni H, AlFaify S. Influence of rare earth material (Sm^{3+}) doping on the properties of electrodeposited Cu_2O films for optoelectronics. Journal of Materials Science Materials in Electronics, 2019, 30(3): 2530–2537
32. Kim J, Choi W, Park J W, Kim C, Kim M, Song H. Branched copper oxide nanoparticles induce highly selective ethylene production by electrochemical carbon dioxide reduction. Journal of the American Chemical Society, 2019, 141(17): 6986–6994
33. Zhang Y, Dong L Z, Li S, Huang X, Chang J N, Wang J H, Zhou

J, Li S L, Lan Y Q. Coordination environment dependent selectivity of single-site-Cu enriched crystalline porous catalysts in CO_2 reduction to CH_4. Nature Communications, 2021, 12(1): 6390

34. Montoya J H, Shi C, Chan K, Nørskov J K. Theoretical insights into a CO dimerization mechanism in CO_2 electroreduction. Journal of Physical Chemistry Letters, 2015, 6(11): 2032–2037
35. Ma W, He X, Wang W, Xie S, Zhang Q, Wang Y. Electrocatalytic reduction of CO_2 and CO to multi-carbon compounds over Cu-based catalysts. Chemical Society Reviews, 2021, 50(23): 12897–12914
36. Kortlever R, Shen J, Schouten K J P, Calle-Vallejo F, Koper M T. Catalysts and reaction pathways for the electrochemical reduction of carbon dioxide. Journal of Physical Chemistry Letters, 2015, 6(20): 4073–4082
37. Zhi X, Vasileff A, Zheng Y, Jiao Y, Qiao S Z. Role of oxygen-bound reaction intermediates in selective electrochemical CO_2 reduction. Energy & Environmental Science, 2021, 14(7): 3912–3930
38. Ma W, Xie S, Zhang B, He X, Liu X, Mei B, Sun F, Jiang Z, Lin L, Zhang Q, et al. Copper lattice tension boosts full-cell CO electrolysis to multi-carbon olefins and oxygenates. Chem, 2023, 9(8): 2161–2177
39. Droog J M, Schlenter B. Oxygen electrosorption on copper single crystal electrodes in sodium hydroxide solution. Journal of Electroanalytical Chemistry and Interfacial Electrochemistry, 1980, 112(2): 387–390
40. Zhang G, Zhao Z J, Cheng D, Li H, Yu J, Wang Q, Gao H, Guo J, Wang H, Ozin G A, et al. Efficient CO_2 electroreduction on facet-selective copper films with high conversion rate. Nature Communications, 2021, 12(1): 5745